## PAPER

Check for updates

# An *in situ* generated 3D porous nanostructure on 2D nanosheets to boost the oxygen evolution reaction for water-splitting†

Wenli Yu,[a] Zhi Chen,[b] Ying Zhao,[b] Yuxiao Gao,[b] Weiping Xiao,[c] Bin Dong, [ID] *[a] Zexing Wu [ID] *[b] and Lei Wang [ID] *[b]

Efficient oxygen evolution reaction (OER) electrocatalysts can accelerate the reaction kinetics of water-splitting for large-scale hydrogen generation. In this work, 2D nanosheets decorated with a 3D porous nanostructure, including Fe, Co and Ni elements, are developed *via* anodic cyclic voltammetry scanning (ACVs) in the presence of sodium sulfide (FeCoNi-NS-ACVs). The formed 2D nanosheets provide metal ions during ACVs to generate a 3D porous structure and also construct a hierarchical morphology to favor the transport of the electrolyte and release of produced gas bubbles. What's more, the developed FeCoNi-NS-ACVs possesses superhydrophilic and excellent electroconductivity properties. Benefiting from the above merits, FeCoNi-NS-ACVs exhibits excellent electrocatalytic performances for the OER with low overpotentials of 170 mV and 198 mV to drive 50 mA cm$^{-2}$ and 100 mA cm$^{-2}$, respectively, with a small Tafel slope of 64 mV dec$^{-1}$ and remarkable durability over 50 h. Moreover, the FeCoNi-NS-ACVs also exhibits outstanding electrocatalytic activity and stability toward overall water-splitting.

## Introduction

With the ever-increasing environmental contamination caused by the usage of fossil fuels, it is of significance to exploit sustainable and green energies.[1–4] Among them, hydrogen energy is identified as an ideal energy storage medium to alleviate the environmental pollution and energy crisis, owing to its high energy density and eco-friendly features.[5–9] Compared with the traditional synthetic technologies, electrocatalytic overall water-splitting is the most eco-friendly and desired avenue to produce hydrogen energy without the generation of polluted gases.[10–13] However, the electrocatalytic efficiency is limited by the sluggish reaction kinetics on the electrodes, especially the oxygen evolution reaction (OER).[14–19] At present, Ru-based nanomaterials are the most efficient electrocatalysts to over-

come the energy barriers.[20,21] Nevertheless, the high cost combined with scarcity prevented their further large-scale implementation.[22–24] Thus, tremendous efforts have been devoted to exploring efficient and non-precious metal-derived catalysts with specific nanostructures for the OER.[25–28]

Among the investigated nanostructures, 2D nanosheets, as a kind of fascinating nanostructure, possess abundant exposed active sites, an ultrathin morphology and rapid charge mobility and can be utilized as an ideal platform to construct electrocatalysts.[29–32] A 3D porous structure also favors the improvement of the electrocatalytic performance owing to the abundant exposed active sites during the electrocatalytic process.[23–35] Moreover, abundant channels benefit the transport of the electrolyte and release of generated gases and then accelerate the reaction kinetics.[36,37] Therefore, the designed electrocatalyst containing both 2D and 3D morphologies would be a promising avenue to promote the catalytic activity. Apart from the nanostructure, the coupling effects between different metal ions are also a valuable strategy to enhance the electrocatalytic performance. For instance, Zhang's group synthesized a tannin–NiFe (TANF) complex film on carbon fiber paper by a facile deposition method used for catalyzing the OER efficiently with ultra-high mass activity (9.17 × 103 Ag$^{-1}$@300 mV) and rapid OER kinetics. All the TA–metal complexes exhibited the best OER performance compared with TA–Ni and TA–Co. According to their study, it is clear that the performance of the obtained TANF can be further optimized by adjusting the ratio of metals.[38] It is

*[a] State Key Laboratory of Heavy Oil Processing, College of Science, China University of Petroleum (East China), Qingdao 266580, China. E-mail: dongbin@upc.edu.cn*
*[b] Key Laboratory of Eco-chemical Engineering, Taishan Scholar Advantage and Characteristic Discipline Team of Eco Chemical Process and Technology, Qingdao International Cooperation Base of Ecological Chemical industry and Intelligent Manufacturing, College of Chemistry and Molecular Engineering, Qingdao University of Science and Technology, Qingdao 266042, P. R. China.*
*E-mail: splswzx@qust.edu.cn, inorchemwl@126.com*
*[c] College of Science, Nanjing Forestry University, Nanjing, 210037, PR China*
†Electronic supplementary information (ESI) available: SEM images, XRD patterns, XPS spectra, and electrochemical data. See DOI: 10.1039/d1nr08007e

proved that the coupling effect between different metals is a reasonable strategy to prepare high efficiency catalysts.

In this work, we designed trimetallic 2D nanosheets coupled with a 3D nanostructure through corrosion engineering and following ACVs in the presence of sodium sulfide on iron foam (Scheme 1). The constructed specific nanostructure is in favor of exposing active sites, providing abundant channels and facilitating mass transport. Moreover, the designed FeCoNi-NS-ACVs has a superhydrophilic surface and a low electrochemical resistance which play a key role in boosting the electrocatalytic performance. As a result, the developed electrocatalysts exhibit remarkable electrocatalytic performance and stability toward the OER in alkaline media.

# Experimental section

## Synthesis of FeCoNi-NS

First, the Fe foam (2.0 cm × 1.0 cm × 0.1 cm) was pretreated in anhydrous ethanol, acetone, and anhydrous ethanol for 30 min under ultrasonic treatment to clean surface impurities. $Ni(NO_3)_2 \cdot 6H_2O$ (0.14 g), $Co(NO_3)_2 \cdot 6H_2O$ (0.022 g) and terephthalic acid (0.033 g) were dissolved in 15 mL of DMF under magnetic stirring to obtain a homogeneous solution A. Then 1 mL of deionized water with NaCl (0.035 g) provided solution B. Next, the above two solutions were mixed and transferred to a 100 mL Teflon-lined stainless-steel autoclave reactor with Fe foam. Then it was put into an oven for 3 h at 150 °C and FeCoNi-nanosheets (FeCoNi-NS) were obtained. After that, the FeCoNi-NS were washed with absolute ethanol and deionized water several times to remove unreacted reactants. Finally, the FeCoNi-NS were dried at 60 °C for 12 h. For comparison, FeNi-NS were prepared without $Co(NO_3)_2 \cdot 6H_2O$, FeCo-NS were prepared without $Ni(NO_3)_2 \cdot 6H_2O$, FeCoNi–S were prepared without terephthalic acid, and Fe–S were prepared without $Co(NO_3)_2 \cdot 6H_2O$, $Ni(NO_3)_2 \cdot 6H_2O$ and terephthalic acid. Other samples prepared with different amounts (0, 70 mg, and 140 mg) of NaCl were named 0- NaCl, 70- NaCl, and 140- NaCl, respectively.

## Synthesis of FeCoNi-NS-ACVs

The FeCoNi-NS-ACVs was used as the working electrode with a Pt foil used as the counter electrode and a saturated calomel electrode (SCE) used as the reference electrode. Then, seven cyclic voltammetry (CV) cycles from 0 to 1.3 V vs. SCE in 1 M KOH containing 1.5 g of $Na_2S$ proceeded with a scanning rate of 10 mV s$^{-1}$. For comparison, other samples with different amounts (0, 1.0, and 1.8 g) of $Na_2S$ were named 0- $Na_2S$, 1.0-$Na_2S$, and 1.8- $Na_2S$, respectively. The resulting electrode was denoted as FeCoNi-NS-ACVs which can serve as a working electrode directly for subsequent electrochemical measurements.

## The HER electrode synthesis of F–FeCoP

$Co(NO_3)_2 \cdot 6H_2O$ and $NH_4F$ were placed in the bottom of the bottle with iron foam added, and placed in the air dryer to react at 120° for 12 h. After that, the reactor was cooled naturally at room temperature, and the precatalyst was washed with absolute ethanol and deionized water several times to remove unreacted reactants. Next, sodium hypophosphite and the precatalyst were, respectively, placed upstream and downstream under an argon atmosphere to obtain F–FeCoP (350 °C, 2 h).

## Physical characterization

The morphologies of all the obtained samples were detected using a scanning electron microscope (SEM) (Hitachi S-4800) and a transmission electron microscope (TEM) (FEI Tecni G20, 200 kV) configured with an energy-dispersive X-ray spectroscope (EDX) for the analysis of the composition and distribution of elements in the samples. The crystal structure information of the samples was provided by X-ray diffraction (XRD) (Rigaku D/max-2500pc device with Cu Kα radiation ($\lambda$ = 1.54 Å)). The Raman spectra of samples were obtained using a LabRAM HR Evolution with an excitation wavelength of 514 nm. The FT-IR spectra (KBr pellets) of samples were obtained using a Thermo Scientific Nicolet-iS10 FT-IR spectrometer. The information on the valence states of the samples was collected by X-ray photoelectron spectroscopy (XPS) carried out using a Thermo Fisher Scientific II spectrometer with an Al Kα source (1486.6 eV). The contents of Ni, Fe, Co and S were measured by inductively coupled plasma emission spectroscopy (ICP) using an Agilent 720 instrument. The contact angle was measured using an OCA15EC tester (DataPhysics, Germany).

## Electrochemical characterization

Electrochemical characterization was performed using an electrochemical station (Gamry Reference 3000) with a typical three-electrode setup in 1.0 M KOH. The electrochemical measurements were performed with a saturated calomel electrode (SCE) and Pt foil which were used as the reference electrode and counter electrode, respectively. All final potentials were given by eqn (1):

$$E(\text{RHE}) = E(\text{SCE}) + E°(\text{SCE}) + 0.059 \text{ pH } (E°(\text{SCE}) = 0.243 \text{ V}) \quad (1)$$

and the overpotential by eqn (2):

$$E°(\text{RHE}) = E(\text{RHE}) - 1.229 \text{ V}. \quad (2)$$

Linear sweep voltammetry (LSV) curves for the OER were obtained with a scanning rate of 10 mV s$^{-1}$. The CV curves of the prepared catalyst in the potential range of 0.2 to 0.3 V (vs.
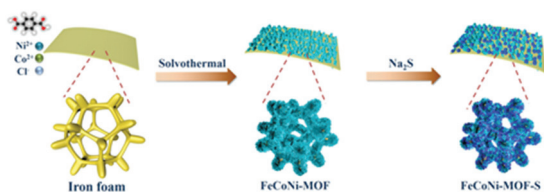


**Scheme 1** Schematic illustration of the synthetic route of FeCoNi-NS-ACVs.

SCE) and in the scan range of 40 to 140 mV s$^{-1}$ were plotted. The frequency of electric impedance spectroscopy (EIS) measurements ranged from 105 to 0.1 Hz with an amplitude of 5 mV. Multiple-step chronopotentiometry and chronopotentiometry measurements for 52 h were used to measure the long-term stability of the sample.

## Results and discussion

The morphologies of the synthesized electrocatalysts were investigated by both SEM and TEM measurements. As shown in Fig. S1 in the ESI,† the iron foam exhibits a smooth surface without specifically decorated nanomaterials and 2D nanosheets formed after solvothermal reaction (Fig. 1(a), S2 in the ESI†). We calculated the thickness of the nanosheet according to the SEM image which is about 15.87 nm (Fig. S3 in the ESI†). Interestingly, the 2D nanosheet morphology was maintained well except for the evolved 3D porous structure after ACVs in the presence of sodium sulfide in 1 M KOH. The specific morphology composed of 2D and 3D nanostructures is beneficial for the transport of the electrolyte, exposing abundant active sites and multiple channels during the electrocatalytic process, and then improving the catalytic performance effectively. However, it is not easy to characterize the specific composition of the 3D porous species due to the intimate contact with the 2D nanosheet (Fig. 1(b), S4 in the ESI†). We believe that the porous species are composed of metal sulfide and metal hydroxide which are generated during ACVs and the metal ions are derived from the 2D nanosheets. That is, the released metal ions from the coordination structure then react with sodium sulfide and hydroxide ions to generate a metal sulfide and a metal hydroxide. The ICP-MS results

(Table S1 in the ESI†) confirmed that the metal ions dissolved in the electrolyte during the ACVs. However, there is almost no 3D structure formed on the surface of both FeNi-NS-ACVs and FeCo-NS-ACVs (Fig. S5 in the ESI†). The XRD pattern demonstrated that the obtained FeCoNi-NS-ACVs is composed of the metal sulfide and metal hydroxide (Fig. S6 in the ESI†). The obtained FeCoNi-NS-ACVs was composed of the metal sulfide and hydroxide. Moreover, the MOF of MIL-53 still existed after ACVs demonstrating its robust nature which plays a pivotal role in exposing abundant active sites and provides rich channels. In order to avoid the diffraction peaks of the iron mesh covering the real active materials, we scraped the electrocatalysts off the iron mesh to conduct the XRD measurements. Then, no peaks were detected in the obtained XRD pattern. The obtained FeCoNi–S, without terephthalic acid addition during the solvothermal process, presents the typical random structure, demonstrating that the ligand plays a significant role in regulating the morphologies (Fig. S7 in the ESI†). The nanosheet can be also clearly observed from the TEM image (Fig. 1(c) and (d)), and the high-resolution TEM image presents the interplanar spacings of 0.213 nm, 0.207 nm and 0.231 nm corresponding to the (121) facet of CoOOH, (131) facet of FeOOH, and (002) facet of Ni(OH)$_2$, respectively (Fig. 1(e)). Moreover, the elemental mappings demonstrated the presence of Ni, Co, Fe, S, O and C elements in the prepared FeCoNi-NS-ACVs (Fig. 1(g)). The N$_2$ adsorption–desorption curves of catalysts reveal that the catalysts possess a mesoporous structure (Fig. S8 in the ESI†). It was observed that the BET surface area of FeCoNi-NS-ACVs (6.25 m$^2$ g$^{-1}$) is larger than that of the 2D nanosheets (5.36 m$^2$ g$^{-1}$), implying that the 3D porous species can improve the surface area of materials. Based on the pore size distribution, the pores on FeCoNi-NS-ACVs mainly center at 14.16 nm which is similar to that of FeCoNi-NS (13.61 nm). The results confirmed the mesoporous structure of catalysts which is in favour of exposing more catalytic sites and promoting the mass transfer rate.

XPS measurements verified the presence of C, S, O, Fe, Co, and Ni elements in the as-designed FeCoNi-NS-ACVs (Fig. S9 in the ESI†). For high-resolution Fe 2p (Fig. 2(a)), the peaks
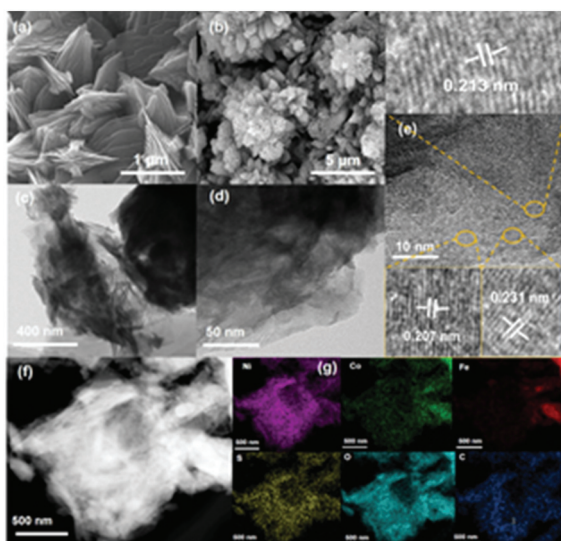


**Fig. 1** (a) SEM morphologies of FeCoNi-NS. (b) SEM image, (c and d) TEM images, (e) HRTEM image, (f and g) HAADF–STEM image and the corresponding element mappings of Fe, Co, Ni, S, C, and O in FeCoNi-NS-ACVs.



**Fig. 2** XPS survey spectra of Fe 2p (a), Ni 2p (b), Co 2p (c) and S 2p (d) of the designed FeCoNi-NS-ACVs. (e) Raman spectra of FeCoNi-NS and FeCoNi-NS-ACVs. (f) Contact angle measurement of FeCoNi-NS-ACVs.

located at 723.2 eV, 711.5 eV and 726.6 eV, 713.9 eV are ascribed to $Fe^{2+}$ and $Fe^{3+}$, respectively.[39–41] As illustrated in Fig. 2b, $Ni^{2+}$ and $Ni^{3+}$ are discovered in the as-prepared FeCoNi-NS-ACVs, where the peaks are located at 875.1 eV, 857.1 eV and 873.2 eV, 855.6 eV, respectively.[39,42] Also, the peaks at 784.4 eV, 774.7 eV and 781.0 eV are ascribed to the characteristic species of $Co_2^+$ and $Co^{3+}$ (Fig. 2(c)).[41,42] We studied the XPS of FeCo-NS-ACVs and FeNi-NS-ACVs to study the electronic interactions. In Fe 2p, FeCoNi-NS-ACVs shifts to high binding energy after the introduction of the third element demonstrating the electronic interactions and then plays a pivotal role in promoting the electrocatalytic performance (Fig. S10 in the ESI†).[43] The high-resolution S 2p data show three types of peaks, and the peak at 168.4 eV corresponds to S–O and those at 163.8 eV and 162.1 eV correspond to the M–S bonds (Fig. 2(d)), demonstrating the successful synthesis of metal sulfide during ACVs.[44–46] The researchers found that the OER properties of transition metal divalent cations follow the order $Fe^{2+} < Co_2^+ < Ni^{2+}$.[47] It is widely recognized that small amounts of iron can effectively increase the catalytic activity of Ni- and Co-based catalysts.[48–50] Therefore, in this experiment, we added a small amount of NaCl to partially corrode the IF mesh and release the iron ion. The Ni species was used as the major active site to optimize electron distribution and transfer, and other elements (Fe and Co) were used to regulate the intrinsic activity of the catalyst.[51] In addition, the XPS spectra of Fe 2p were shifted by the incorporation of cobalt. In a word, the addition of the third element will act as an electronic regulator for any two existing elements, causing the redistribution of electrons, and finally, the sample exhibiting the tri-metal has the best OER activity. Raman measurements were conducted to investigate the nanostructure evolution after ACVs. As shown in Fig. 2(e), two new peaks at 483.3 $cm^{-1}$ and 686.5 $cm^{-1}$ were generated after ACVs, which are associated with metal hydroxide and generally considered as the active species during the OER.[38,52–56] Moreover, the surface properties of the as-developed electrocatalyst also play a pivotal role in the electrocatalytic process. As shown in Fig. 2(f) and Movie S1,† the prepared FeCoNi-NS-ACVs exhibits superhydrophilic properties and then it can come in contact with the electrolyte intimately to accelerate the reaction kinetics which is better than that of IF and FeCoNi-NS (Fig. S11 in the ESI and Movie S2 in the ESI†).

The electrocatalytic OER performances of the as-prepared FeCoNi-NS-ACVs and reference samples are conducted in 1 M KOH *via* a typical three-electrode setup. As shown in Fig. 3(a and b), the polarization potentials required to attain 50 mA $cm^{-2}$ and 100 mA $cm^{-2}$ of FeCoNi-NS-ACVs are 170 mV and 198 mV, respectively, which are superior to those of the $RuO_2$ benchmark catalyst and some of the reported values (Fig. 3(c) and Tables S2 and S3 in the ESI†). The bimetallic FeNi-NS-ACVs and FeCo-NS-ACVs exhibit poor catalytic activities with higher overpotentials relative to the trimetallic FeCoNi-NS-ACVs, demonstrating that the coupling effects of the introduced metal species play a crucial role in promoting the catalytic performance. In addition, the prepared FeCoNi–S pos-
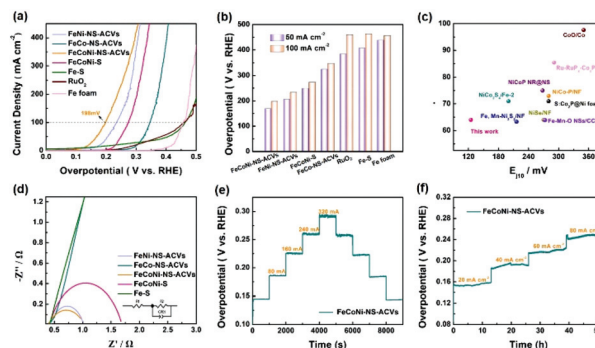


Fig. 3 Electrochemical measurements: (a) OER polarization curves, (b) overpotential comparison at 50 mA $cm^{-2}$ and 100 mA $cm^{-2}$, (c) comparison of the overpotentials (Ej10) and Tafel slopes with the references, (d) Nyquist plots, and (e and f) stability tests of the obtained catalysts in 1 M KOH.

sesses larger overpotentials (250 mV@50 mA $cm^{-2}$ and 273 mV@100 mA $cm^{-2}$) relative to FeCoNi-NS-ACVs in the studied potential range. The Tafel plots (Fig. S12 in the ESI†) verified that FeCoNi-NS-ACVs possesses a smaller value (64 mV $dec^{-1}$) than FeCoNi–S (78 mV $dec^{-1}$), indicating the faster kinetics of the electrode containing nanosheets. Therefore, the constructed 2D nanosheet plays a pivotal role in boosting the catalytic process, owing to the specific nanostructure benefiting the transport of the electrolyte and release of generated gas bubbles.

In addition, it is identified that the electrochemical surface area is an important factor reflecting the intrinsic activity of catalysts which is estimated from the $C_{dl}$ value. The double-layered capacitance ($C_{dl}$) of the catalyst was measured by cyclic voltammetry with different scan rates (Fig. S13†). FeCoNi-NS-ACVs possesses a high $C_{dl}$ value (26.7 mF $cm^{-2}$), which is favorable to boosting the OER activity. The electrochemical impedance spectroscopy (EIS) results of the synthesized samples are shown in Fig. 3(d) and Table S4 in the ESI.† It is well-known that the conductivity of the catalytic electrode directly influences the electrocatalytic activity. The conductivity of the catalytic electrode is the best among the prepared electrocatalysts. Evidently, the as-prepared FeCoNi-NS-ACVs displays the smallest Nyquist semicircle diameter, demonstrating the lowest resistance of charge transfer during the electrocatalytic OER process. It is widely recognized that small amounts of iron can effectively increase the catalytic activity of Ni- and Co-based catalysts.[48–50] Therefore, the generated iron species *via* a corrosive process play a significant role in promoting the catalytic activity. Moreover, the coupling effects, such as electronic interactions, between different elements also accelerate the reaction kinetics effectively. As a key factor, the electrochemical conductivity would affect the electron/charge transfer during the electrocatalytic process. As revealed by the obtained results, the designed tri-metallic electrocatalysts exhibit the lowest electrochemical resistance, thus improving the catalytic performance effectively. Therefore, the excellent OER performance is due to the coupling effects

between different elements and the specific nanostructure. Except for the remarkable catalytic activity, the developed FeCoNi-NS-ACVs also possesses excellent long-term stability. As depicted in Fig. 3(e) and (f),† the current densities increased with the increase of applied potentials, and then the current densities were maintained well during the reverse process, indicating its outstanding stability.

As has been mentioned, the obtained FeCoNi-NS-ACVs exhibits long term stability toward the OER for over 50 h. Then, we investigated its properties after the stability test by SEM and XPS measurements. As shown in Fig. 4(a) and (b) and S14 in the ESI,† the obtained FeCoNi-NS-ACVs maintained the 3D porous structure well after the stability test, indicating its robust nanostructure. For XPS (Fig. 4(c)–(f), S15 in the ESI†), the XPS pattern of FeCoNi-NS-ACVs shows no obvious losses after the OER test which provides evidence that it has no structural changes, proving that it is extremely stable. Thus, all the tests have confirmed the great potential of FeCoNi-NS-ACVs as a practical electrocatalyst for the OER. As a key factor, we investigated the mass content of NaCl in regulating the electrocatalytic activity for the OER (Fig. S16 in the ESI†). The presence of NaCl plays a vital role in regulating the electrocatalytic performance owing to the $Cl^-$ ions, which can corrode the iron foam during the solvothermal process and the leached iron ion forms the electrocatalyst. The results show that the electrocatalyst with 35 mg NaCl exhibits the lowest overpotential and Tafel slope. Moreover, we also studied the effects of $Na_2S$ on tuning the electrocatalytic performance (Fig. S17 in the ESI†). Obviously, the content of $Na_2S$ also regulated the electrocatalytic activity and the optimal value is 1.5 g with a small overpotential and Tafel slope.

Thanks to the excellent electrocatalytic activity toward the OER, a full water-splitting setup is built with the prepared FeCoNi-NS-ACVs and F–FeCoP as the anode and cathode, respectively. As illustrated in Fig. 5(a), low voltages of 1.37 V and 1.58 V are needed to reach 10 mA cm$^{-2}$ and 100 mA cm$^{-2}$, respectively, superior to many other available catalysts (Fig. 5(e) and Table S5 in the ESI†). Owing to the small voltage, the overall water-splitting configuration is easily powered by sustainable and intermittent solar energy and sumless
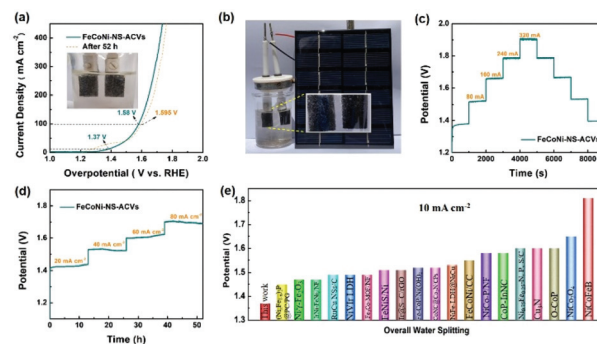


**Fig. 5** (a) LSV curves of FeCoNi-NS-ACVs//F–FeCoP and the catalyst after 52 h stability test for overall water splitting in 1 M KOH (the inset is an image of the water splitting cell). (b) Solar cell driving overall water-splitting. (c and d) Stability tests of the obtained catalysts in 1 M KOH. (e) Comparison of the overpotentials (Ej10) with the references.

bubbles generated on the electrodes (Fig. 5(b) and Movie S3 in the ESI†). Moreover, the designed FeCoNi-NS-ACVs also exhibits excellent stability for overall water-splitting, which is confirmed *via* multi-step measurements (Fig. 5(c) and (d)). As discussed above, the developed trimetallic nanosheet derived nanomaterial shows remarkable electrocatalytic performance which can be attributed to the following factors: the specific nanostructure constructed by 2D and 3D morphologies can expose abundant active sites and benefit the transport of the electrolyte; the coupling effects of the introduced metal species also play a significant role in improving the catalytic activity; the superhydrophilic and low electrochemical resistance properties are key factors during the electrocatalytic process; the iron foam substrate with a porous nanostructure provides rich channels for the release of generated bubbles.

## Conclusions

In summary, we have developed a 3D nanostructure supported on trimetallic 2D nanosheet nanomaterials *via* corrosion engineering and following ACVs for the OER in alkaline media. The coupling effects between the introduced metal species and the 2D nanosheets play pivotal roles in boosting the electrocatalytic activity. Moreover, the iron foam substrate possessed a porous structure with multiple channels and thus enabled the transport of the electrolyte and timely release of generated bubbles to expose the active sites. Thus, the designed FeCoNi-NS-ACVs presents remarkable electrocatalytic performance and excellent stability toward the OER and overall water-splitting. This work provides a facile and scalable strategy to develop non-precious metal-based nanomaterials for energy-related applications.

## Conflicts of interest
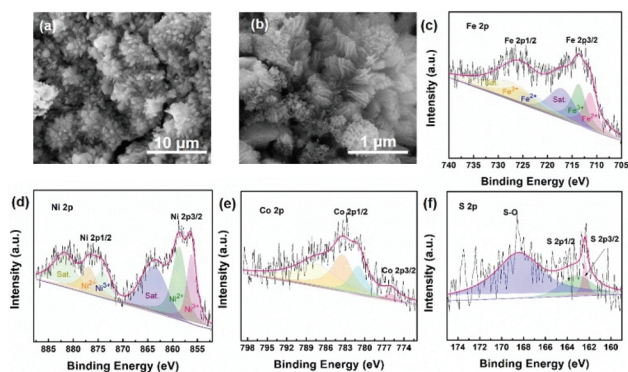
There are no conflicts to declare.



**Fig. 4** SEM image (a) and (b), XPS survey spectra of Fe (c), Ni (d), Co (e) and S (f) of FeCoNi-NS-ACVs after a long-time stability test.

# Acknowledgements

# Notes and references

1 H. Yang, L. Gong, H. Wang, C. Dong, J. Wang, K. Qi, H. Liu, X. Guo and B. Y. Xia, *Nat. Commun.*, 2020, **11**, 5075.

2 G. Zhao, W. X. Ma, X. K. Wang, Y. P. Xing, S. H. Hao and X. J. Xu, *Adv. Powder Mater.*, 2021, DOI: 10.1016/j.apmate.2021.09.008.

3 J. R. Yang, W. H. Li, D. S. Wang and Y. D. Li, *Adv. Mater.*, 2020, **32**, 2003300.

4 J. Luo, W. H. Guo, Q. Zhang, X. H. Wang, L. Shen, H. C. Fu, L. L. Wu, X. H. Chen, H. Q. Luo and N. B. Li, *Nanoscale*, 2020, **12**, 19992–20001.

5 H. Y. Jing, P. Zhu, X. B. Zheng, Z. D. Zhang, D. S. Wang and Y. D. Li, *Adv. Powder Mater.*, 2021, DOI: 10.1016/j.apmate.2021.10.004.

6 J. D. Wu, D. P. Wang, S. A. Wan, H. L. Liu, C. Wang and X. Wang, *Small*, 2020, **16**, 1900550.

7 D. Yang, W. Hou, Y. Lu, W. Zhang and Y. Chen, *Nanoscale*, 2019, **11**, 12837–12845.

8 B. Wang, C. Tang, H. F. Wang, X. Chen, R. Cao and Q. Zhang, *Adv. Mater.*, 2019, **31**, 1805658.

9 P. F. Cheng, T. Feng, Z. W. Liu, D. Y. Wu and J. Yang, *Chin. J. Catal.*, 2019, **40**, 1147–1152.

10 C. Tang, Y. Jiao, B. Shi, J. N. Liu, Z. Xie, X. Chen, Q. Zhang and S. Z. Qiao, *Angew. Chem., Int. Ed.*, 2020, **59**, 9171–9176.

11 Z. X. Wu, D. Z. Nie, M. Song, T. T. Jiao, G. T. Fu and X. Liu, *Nanoscale*, 2019, **11**, 7506–7512.

12 Z. Chen, D. Z. Liu, Y. X. Gao, Y. Zhao, W. P. Xiao, G. R. Xu, T. Y. Ma, Z. X. Wu and L. Wang, *Sci. China Mater.*, 2022, DOI: 10.1007/s40843-021-1943-5.

13 L. Q. Gong, H. Yang, H. M. Wang, R. J. Qi, J. L. Wang, S. H. Chen, B. You, Z. H. Dong, H. F. Liu and B. Y. Xia, *Nano Res.*, 2021, **14**, 4528–4533.

14 Z. X. Wu, H. B. Wu, T. F. Niu, S. Wang, G. T. Fu, W. Jin and T. Y. Ma, *ACS Sustainable Chem. Eng.*, 2020, **8**, 9226–9234.

15 Z. J. Li, X. D. Wu, X. Jiang, B. B. Shen, Z. S. Teng, D. M. Sun, G. T. Fu and Y. W. Tang, *Adv. Powder Mater.*, 2021, DOI: 10.1016/j.apmate.2021.11.007.

16 Y. Z. Wen, T. Yang, C. Q. Cheng, X. R. Zhao, E. Z. Liu and J. Yang, *Chin. J. Catal.*, 2020, **41**, 1161–1167.

17 H. Jin, X. Liu, S. Chen, A. Vasileff, L. Li, Y. Jiao, L. Song, Y. Zheng and S. Z. Qiao, *ACS Energy Lett.*, 2019, **4**, 805–810.

18 S. Z. Li, J. Y. Liu, S. Duan, T. Y. Wang and Q. Li, *Chin. J. Catal.*, 2020, **41**, 847–852.

19 W. Q. Feng, H. Chen, Q. Zhang, R. Q. Gao and X. X. Zou, *Chin. J. Catal.*, 2020, **41**, 1692–1697.

20 J. Y. Zhang, Y. Yan, B. Mei, R. Qi, T. He, Z. Wang, W. Fang, S. Zaman, Y. Su, S. Ding and B. Y. Xia, *Energy Environ. Sci.*, 2021, **14**, 365–373.

21 J. J. Mao, C. T. He, J. J. Pei, Y. Liu, J. Li, W. X. Chen, D. S. He, D. S. Wang and Y. D. Li, *Nano Lett.*, 2020, **20**, 3442–3448.

22 X. Liu, Y. Yao, H. Zhang, L. Pan, C. Shi, X. Zhang, Z. F. Huang and J. J. Zou, *ACS Sustainable Chem. Eng.*, 2020, **8**, 17828–17838.

23 L. R. Bao, S. H. Zhu, Y. Chen, Y. Wang, W. H. Meng, S. Xu, Z. H. Lin, X. Y. Li, M. Sun and L. M. Guo, *Fuel*, 2022, **314**, 122774.

24 W. Cheng, S. Xi, Z.-P. Wu, D. Luan and X. W. Lou, *Sci. Adv.*, 2021, **7**(46), eabk0919.

25 T. Zhang, B. Zhang, Q. Peng, J. Zhou and Z. M. Sun, *J. Mater. Chem. A*, 2021, **9**, 433–441.

26 Z.-P. Wu, H. Zhang, S. Zuo, Y. Wang, S. L. Zhang, J. Zhang, S.-Q. Zang and X. W. Lou, *Adv. Mater.*, 2021, **33**, 2103004.

27 M. Li, H. Li, X. Jiang, M. Jiang, X. Zhan, G. Fu, J. M. Lee and Y. Tang, *J. Mater. Chem. A*, 2021, **9**, 2999–3006.

28 D. Guo, J. Wang, L. Zhang, X. Chen, Z. Wan and B. Xi, *Small*, 2020, **6**, e2002432.

29 M. K. Cai, Q. L. Liu, Z. Q. Xue, Y. L. Li, Y. N. Fan, A. P. Huang, M. R. Li, M. Croft, T. Tyson, Z. F. Ke and G. Q. Li, *J. Mater. Chem. A*, 2020, **8**, 190–195.

30 W. S. Fang, L. Huang, S. Zaman, Z. Wang, Y. J. Han and B. Y. Xia, *Chem. Res. Chin. Univ.*, 2020, **36**, 611–621.

31 W. B. Chen, C. S. Wang, S. B. Su, H. Wang and D. D. Cai, *Chem. Eng. J.*, 2021, **414**, 128784.

32 R. Yu, D. M. Liu, M. Y. Yuan, Y. Wang, C. Q. Ye, J. Li and Y. K. Du, *J. Colloid Interface Sci.*, 2021, **602**, 612–618.

33 Y. Pei, Y. C. Ge, H. Chu, W. Smith, P. Dong, P. M. Ajayan, M. X. Ye and J. F. Shen, *Appl. Catal., B*, 2019, **244**, 583–593.

34 W. Li, X. S. Chu, F. Wang, Y. Y. Dang, X. Y. Liu, X. C. Wang and C. Y. Wang, *Appl. Catal., B*, 2021, **288**, 120034.

35 Z. P. Lv, W. S. Ma, M. Wang, J. Dang, K. L. Jian, D. Liu and D. J. Huang, *Adv. Funct. Mater.*, 2021, **31**, 2102576.

36 J. J. Xu, J. Q. He, W. Ding, Z. L. Hong and F. Q. Huang, *Adv. Energy Mater.*, 2019, **9**, 1900170.

37 C. Z. Wei, R. Zhang, X. Zheng, Q. L. Ru, Q. Y. Chen, C. Cui, G. Li and D. J. Zhang, *Inorg. Chem. Front.*, 2018, **5**, 3126–3134.

38  Y. M. Shi, Y. Yu, Y. Liang, Y. H. Du and B. Zhang, *Angew. Chem., Int. Ed.*, 2019, **58**, 3769–3773.

39  P. Thangavela, G. Kimb and K. S. Kima, *J. Mater. Chem. A*, 2021, **9**, 14043–14051.

40  L. Yu, H. Q. Zhou, J. Y. Sun, F. Qin, F. Yu, J. M. Bao, Y. Yu, S. Chen and Z. F. Ren, *Energy Environ. Sci.*, 2017, **10**, 1820–1827.

41  Z. K. Shi, Z. B. Yu, R. H. Jiang, J. Huang, Y. P. Hou, J. H. Chen, Y. Q. Zhang, H. X. Zhu, B. Wang and H. Pang, *J. Mater. Chem. A*, 2021, **9**, 11415–11426.

42  F. L. Li, Q. Shao, X. Q. Huang and J. P. Lang, *Angew. Chem., Int. Ed.*, 2018, **57**, 1888–1892.

43  D. Friebel, M. W. Louie, M. Bajdich, K. E. Sanwald, Y. Cai, A. M. Wise, M. J. Cheng, D. Sokaras, T. C. Weng, R. Alonso-Mori, R. C. Davis, J. R. Bargar, J. K. Nørskov, A. Nilsson and A. T. Bell, *J. Am. Chem. Soc.*, 2015, **137**, 1305–1313.

44  J. J. Duan, Z. Han, R. L. Zhang, J. J. Feng, L. Zhang, Q. L. Zhang and A. J. Wang, Iron, *J. Colloid Interface Sci.*, 2021, **588**, 248–256.

45  J. Cao, J. Zhou, Y. Zhang, Y. Wang and X. Liu, *ACS Appl. Mater. Interfaces*, 2018, **10**, 1752–1760.

46  X. Deng, Y. Fan, Q. Zhou, H. Huang, W. Zhou, Z. Lan, X. Liang, G. Li, J. Guo and S. Tang, *Electrochim. Acta*, 2019, **319**, 783–790.

47  R. Subbaraman, D. Tripkovic, K. C. Chang, D. Strmcnik, A. P. Paulikas, P. Hirunsit, M. Chan, J. Greeley, V. Stamenkovic and N. M. Markovic, *Nat. Mater.*, 2012, **11**, 550–557.

48  R. L. Tichenor, *Ind. Eng. Chem.*, 1952, **44**, 973–977.

49  N. Q. Zhang, C. L. Ye, H. Yan, L. C. Li, H. He, D. S. Wang and Y. D. Li, *Nano Res.*, 2020, **13**, 3165–3182.

50  A. Hickling and S. Hill, Oxygen overvoltage. Part I. Discuss, *Faraday Soc.*, 1947, **1**, 236–246.

51  E. Detsi, J. B. Cook, B. K. Lesel, C. L. Turner, Y. L. Liang, S. Robbennolt and S. H. Tolbert, *Energy Environ. Sci.*, 2016, **9**, 540–549.

52  S. J. Lu, W. J. Wang, S. S. Yang, W. Chen, Z. B. Zhuang, W. J. Tang, C. H. He, J. J. Qian, D. K. Ma, Y. Yang and S. M. Huang, *Nano Res.*, 2019, **12**, 3116–3122.

53  M. W. Louie and A. T. Bell, *J. Am. Chem. Soc.*, 2013, **135**, 12329–12337.

54  Y. Wang, L. T. Yan, K. Dastafkan, C. Zhao, X. B. Zhao, Y. Y. Xue, J. M. Huo, S. N. Li and Q. G. Zhai, *Adv. Mater.*, 2021, **33**, 2006351.

55  Z. J. Chen, X. G. Duan, W. Wei, S. B. Wang, Z. J. Zhang and B. J. Ni, *Nano Res.*, 2020, **13**, 293–314.

56  Q. Xu, H. Jiang, H. Zhang, Y. Hu and C. Li, *Appl. Catal., B*, 2019, **242**, 60–66.